Supporting information for

A ^{17}O Paramagnetic NMR Study of Sm_2O_3, Eu_2O_3, and Sm/Eu-substituted CeO_2

Michael A. Hope,[1] David M. Halat,[1,2] Jeongjae Lee,[1] Clare P. Grey[1]

1. Department of Chemistry, University of Cambridge, Lensfield Rd, Cambridge CB2 1EW (UK)
2. Department of Chemical and Biomolecular Engineering, University of California, Berkeley, CA 94720, United States.

1 Summary of NMR Parameters

Table S1: Summary of experimental NMR parameters

Sample	Field /T	Rotor Size /mm	MAS /kHz	Recycle delay /s	RF power /kHz	Acquisition Time	Notes
Sm_2O_3 monoclinic	9.40	1.9	30	0.05	104	10min – 1.5h	$\pi/2$, $\pi/6$ & VT
Eu_2O_3 monoclinic	4.70	1.3	60	0.1	222	5d	
	9.40			0.2 or 1	119	2d – 4d	$\pi/2$ vs. $\pi/6$ and quantification
	9.40	1.9	40 or 35	0.1, 1 or 2	104	1d – 3.5d	SI: VT, T_1 & T_2 comparisons
Sm_2O_3 cubic	9.40	1.9	40	0.05	104	2 min	Room temperature
		4	10		109	1.5 min	Low VT
		7	4		48	7 min	High VT (laser)
Eu_2O_3 cubic	7.05	1.3	40	0.15	167	12.5 min	Room temperature, Avance III
	9.40	4	10		109	1 min	Low VT
		7	3 or 4		48	10 min – 1h	High VT (laser)
Sm-CeO_2	7.05	1.9	40	1	132	30 min	Avance
	4.70	4	14	–	85	1h – 8h	VT T_1
Eu-CeO_2	7.05	1.3	60	1 or 0.1	167	9h	Avance III
			40	–		1h – 4.5h	Avance III, higher VT & T_1
		4	14	–	69	1.25h	Avance III, lower VT T_1
H_2O (natural abundance)	9.40	1.9	–	0.06	104	1.5 h	Enrichment quantification

2 XRD Data and Rietveld Refinements

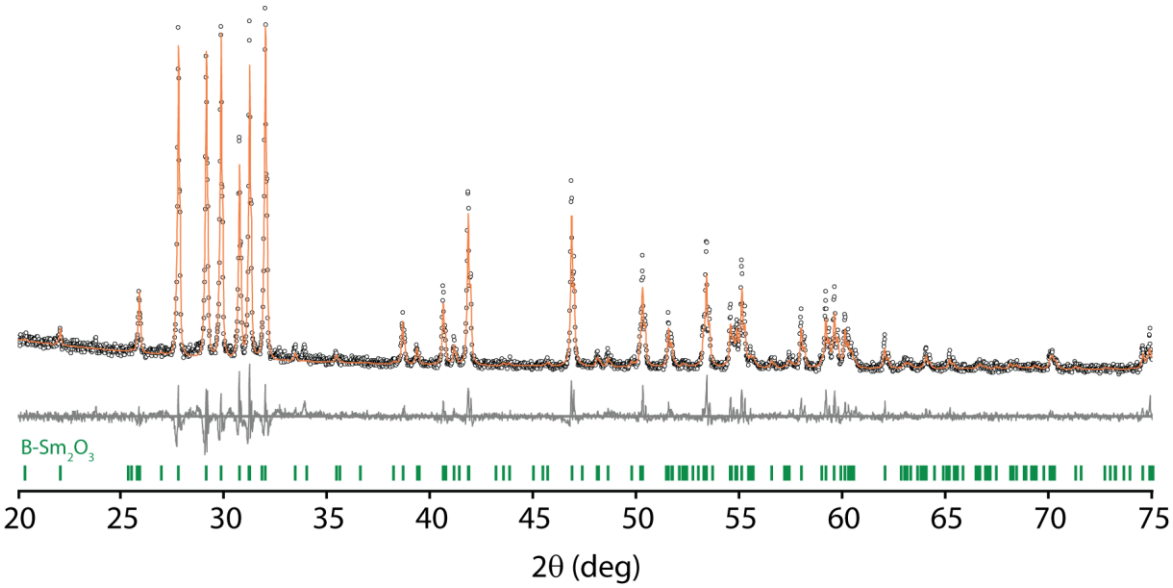

Figure S1: XRD pattern and Rietveld refinement for Sm_2O_3 after ^{17}O enrichment at 1200 °C.

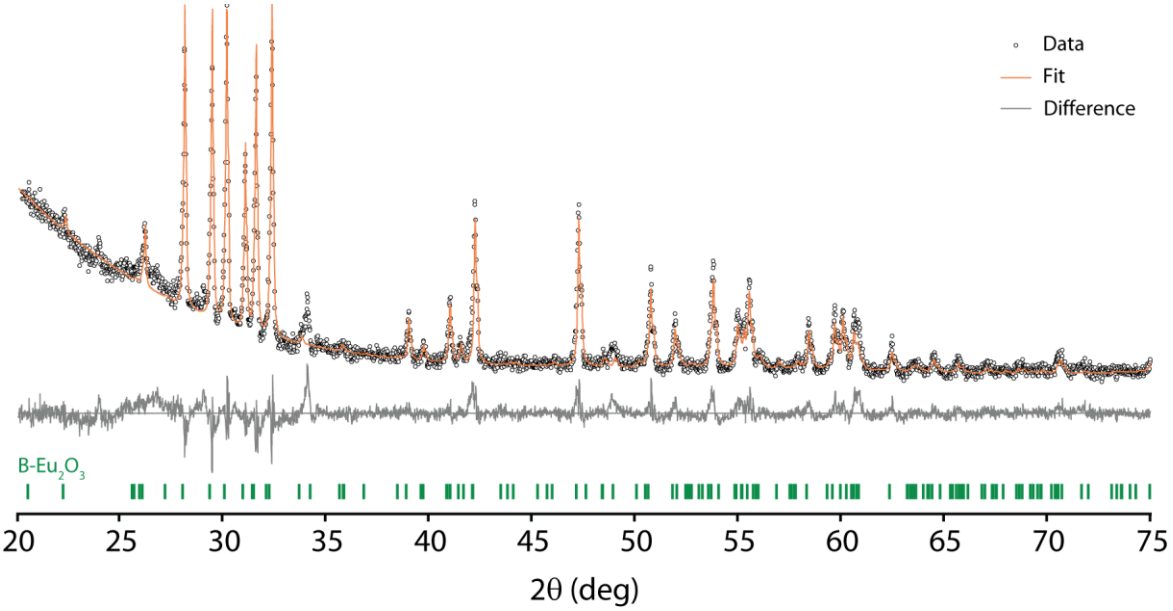

Figure S2: XRD pattern and Rietveld refinement for Eu_2O_3 after ^{17}O enrichment at 1200 °C.

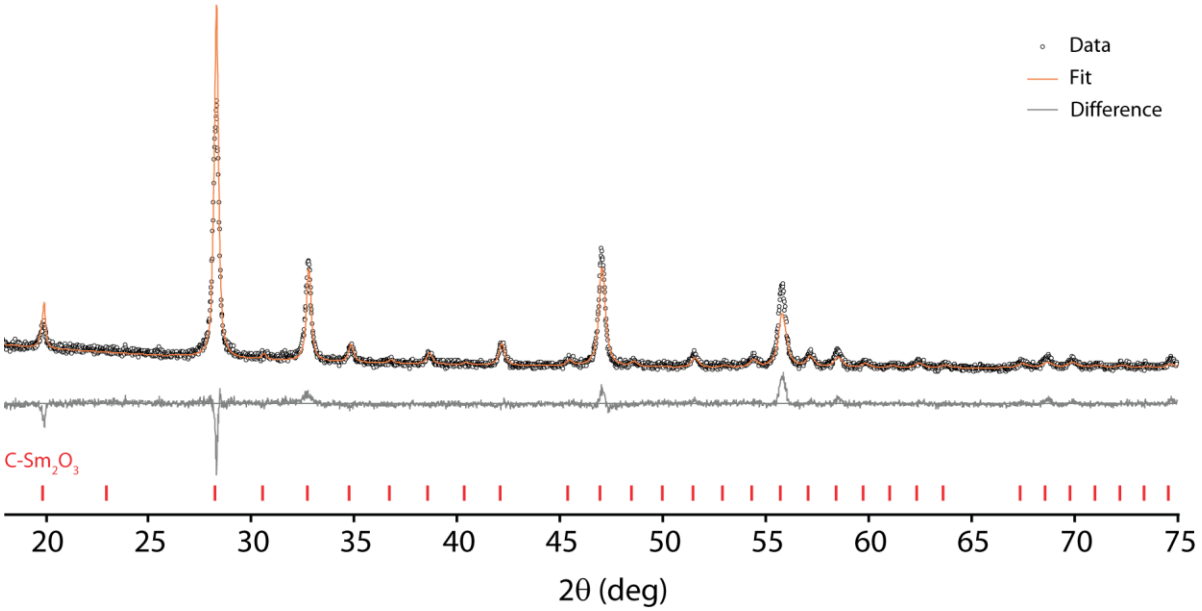

Figure S3: XRD pattern and Rietveld refinement for Sm_2O_3 prepared by decomposing $Sm(OH)_3$ at 750 °C followed by ^{17}O-enrichment at 750 °C.

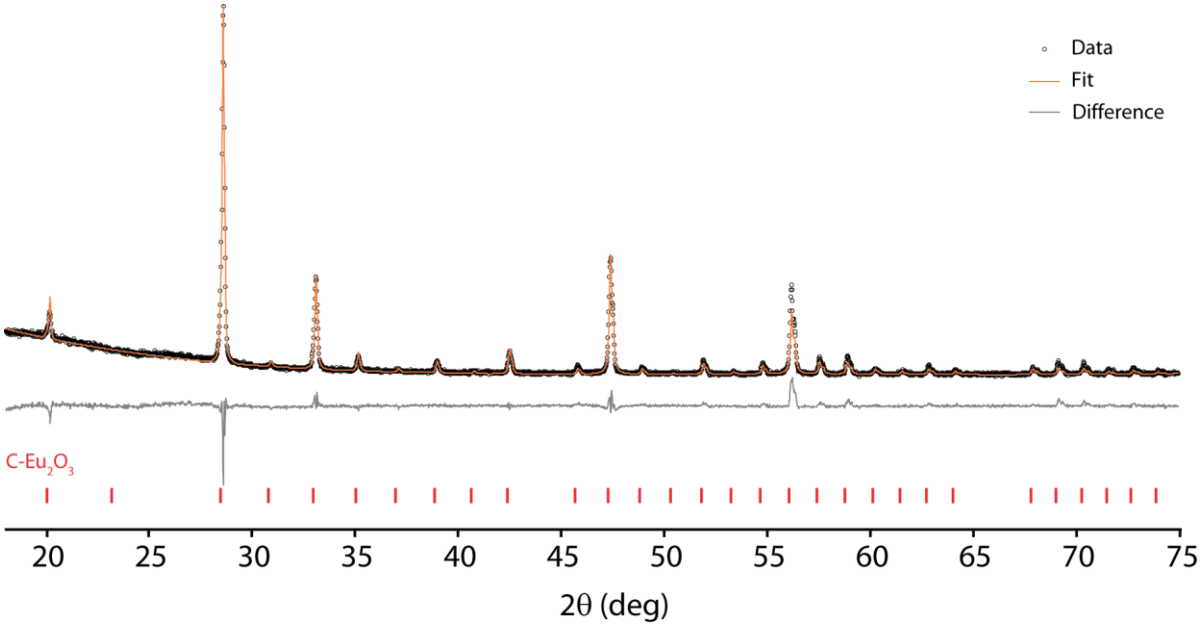

Figure S4: XRD pattern and Rietveld refinement for Eu_2O_3 after ^{17}O enrichment at 1000 °C.

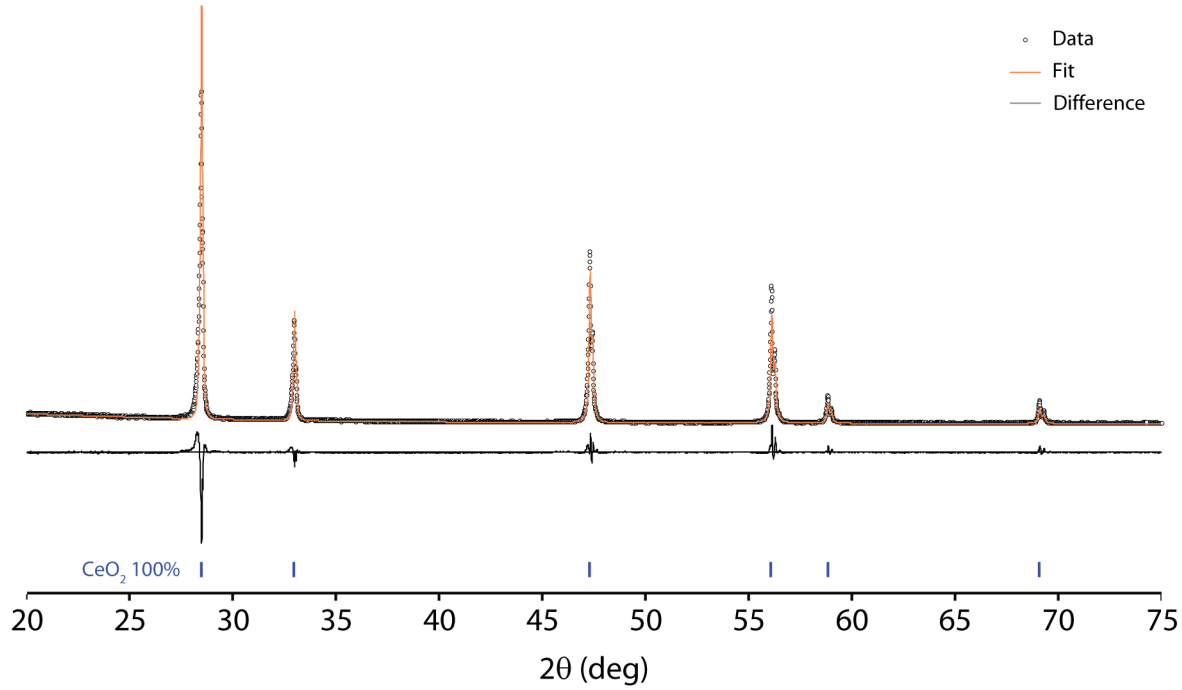

Figure S5: XRD pattern and Rietveld refinement for 15 at% Sm-substituted CeO_2

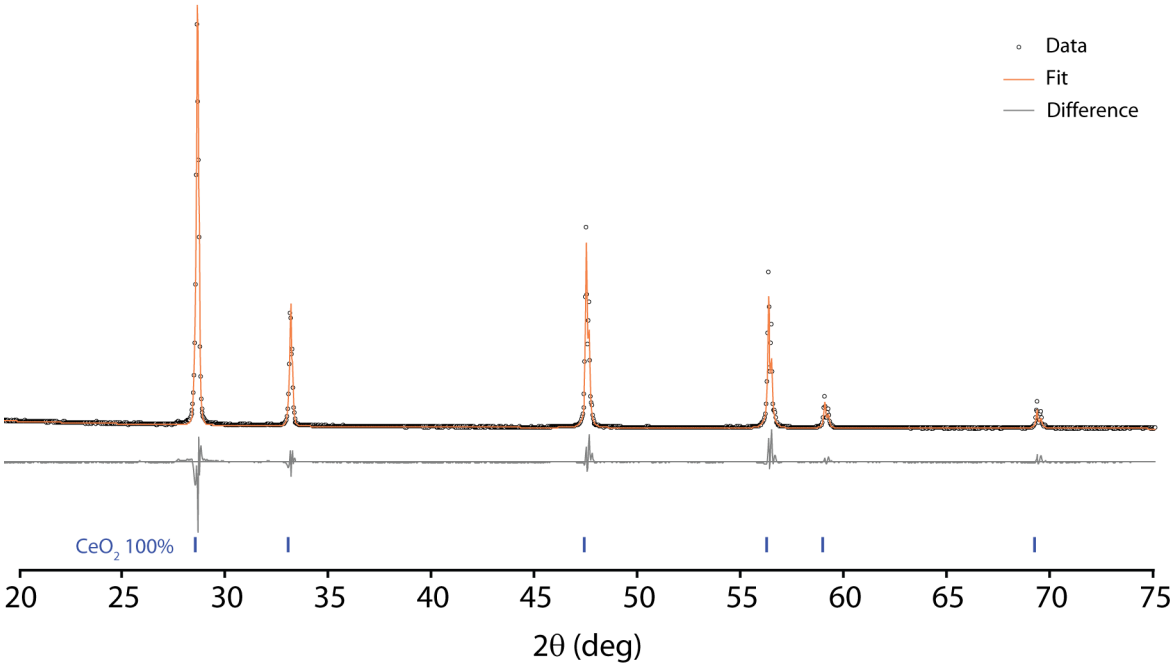

Figure S6: XRD pattern and Rietveld refinement for 15 at% Eu-substituted CeO_2

3 Supplementary NMR Data

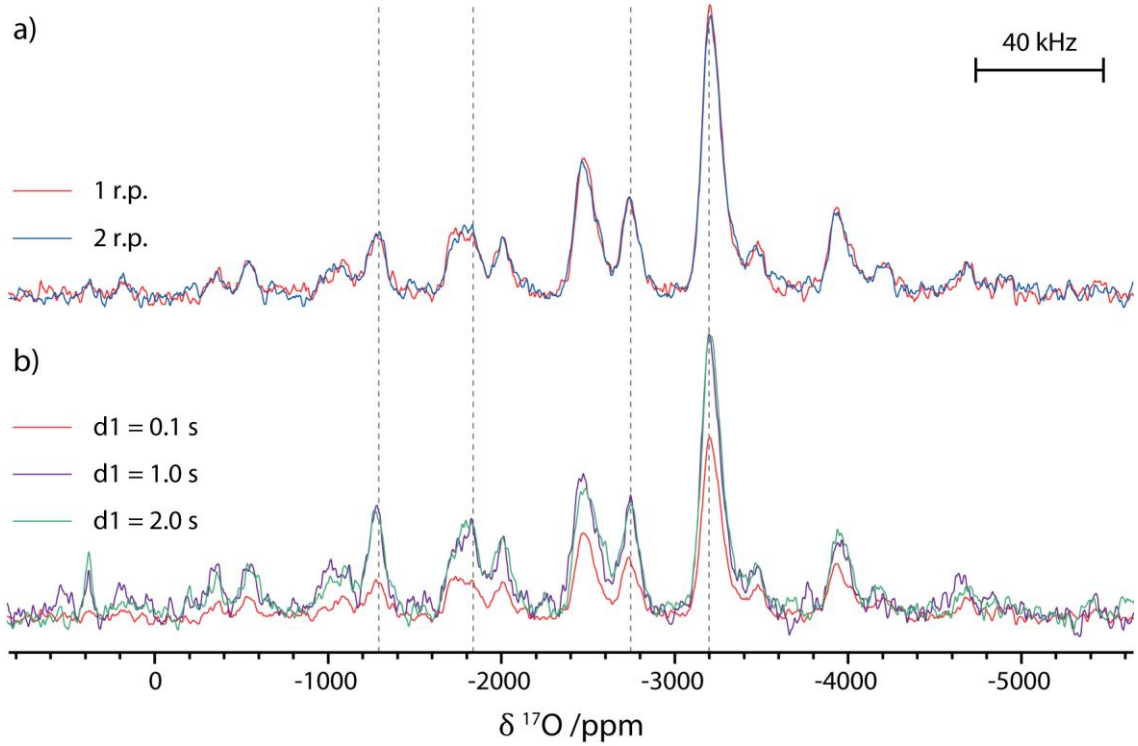

Figure S7: ^{17}O NMR spectra of monoclinic Eu_2O_3 recorded at 9.40 T and 40 kHz MAS using a Hahn echo pulse sequence ($\pi/2$-τ-π-τ-acquire), scaled by the number of scans. Isotropic resonances are marked with dashed lines, although there is significant overlap of the isotropic resonances and spinning sidebands. a) shows a comparison of spectra recorded with echo delays (τ) of either 1 or 2 rotor periods (r.p.) and a 0.1 s recycle delay: there is no significant difference in intensity, indicating that there is not significant T_2 relaxation during the echo. b) shows a comparison of spectra recorded with an echo delay of a single rotor period and recycle delays of 0.1, 1.0 or 2.0 s: this shows that spectra recorded with a recycle delay of 0.1 s are not quantitative, but those with at least 1.0 s are. Furthermore, the T_1 constants appear to be longer for the higher frequency resonances (consistent with these resonances being less paramagnetically shifted); however, the intensity of the lowest frequency resonance is still too great to be ascribed to a single crystallographic site, even accounting for the different T_1 constants.

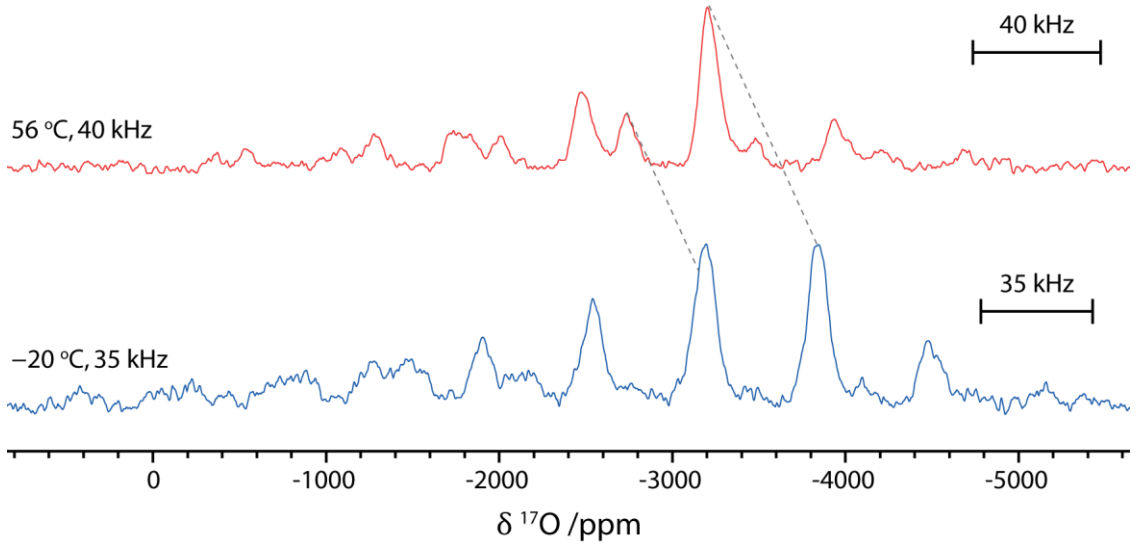

Figure S8: ^{17}O NMR spectra of monoclinic Eu_2O_3 at two different temperatures, recorded at 9.40 T using a Hahn echo pulse sequence and a recycle delay of 0.1 s. At lower temperature, the magnitude of the paramagnetic shifts increases yielding more negative shifts. Unfortunately, this causes the signals at −2780 ppm and −3260 ppm in the higher temperature spectrum to be

spaced by the spinning speed in the lower temperature spectrum so that the sidebands overlap. Nevertheless, it can still be seen that the −3260 ppm resonance does not split into two resonances at the lower temperature.

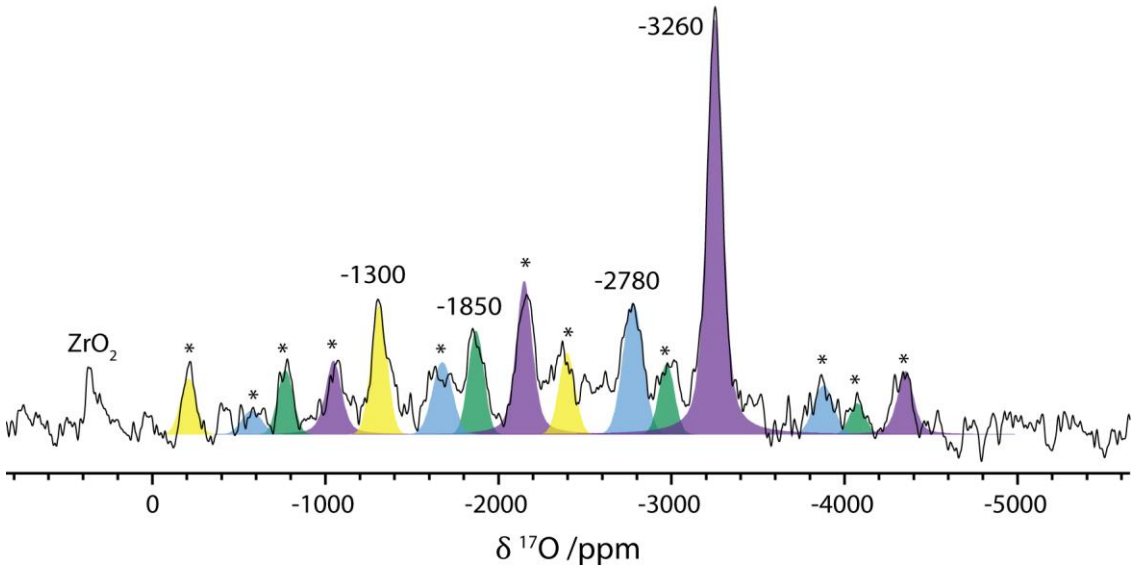

Figure S9: ^{17}O NMR spectrum of monoclinic Eu_2O_3 recorded at 9.40 T and 60 kHz MAS with a quantitative recycle delay of 1 s using a Hahn echo pulse sequence ($\pi/2$-τ-π-τ-acquire). Sidebands are marked with asterisks and the signal from the ZrO_2 rotor is indicated.

Table S2: Calculating the relative integrations of the signals in the ^{17}O NMR spectrum of monoclinic Eu_2O_3, recorded at 60 kHz MAS and 9.05 T. The integrated intensity with an approximately quantitative recycle delay (d1) of 1 s is weighted by the ratio of the amplitudes of each signal recorded with $\pi/2$ and $\pi/6$ pulses, but with recycle delays of 0.2 s, to account for the non-quantitative excitation of $\pi/2$ pulses.

Shift /ppm	**Relative integration π/2, d1 = 1 s**	**Amplitude π/2, d1 = 0.2 s /Arbitrary Units**	**Amplitude π/6, d1 = 0.2 s /Arbitrary Units**	**Ratio of π/6:π/2 Amplitudes**	**Corrected relative integration**
−3260	50%	97.5	14.3	0.15	38%
−2780	20%	20.1	2.8	0.14	14%
−1850	15%	13.6	4.2	0.31	24%
−1300	15%	19.1	5.6	0.30	24%

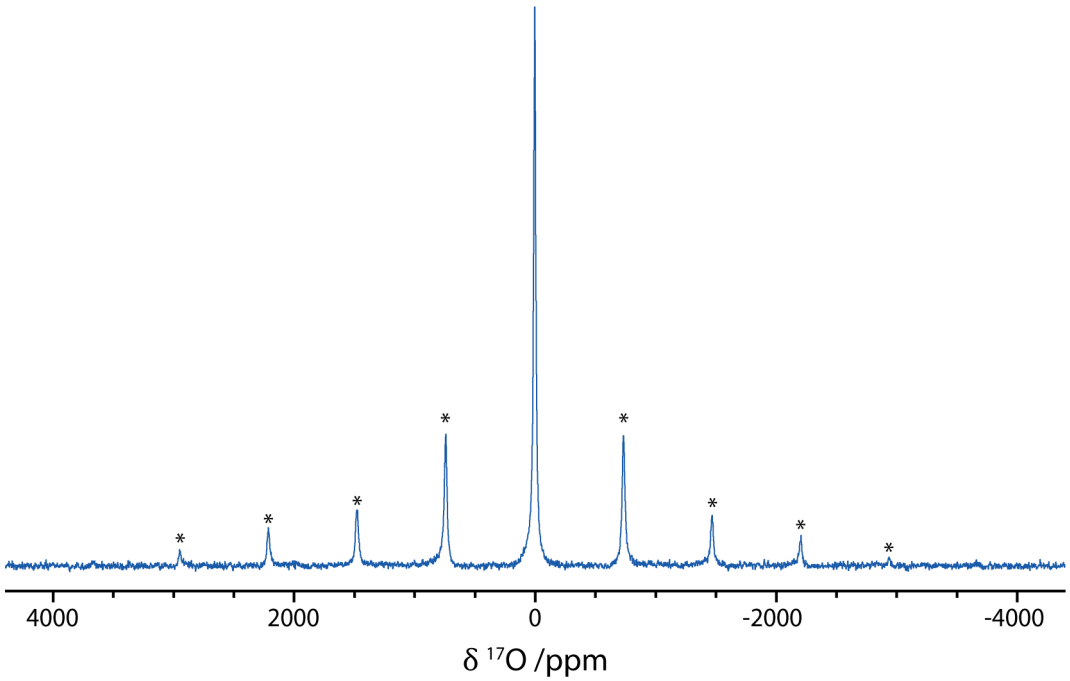

Figure S10: ^{17}O NMR spectrum of cubic Sm_2O_3 recorded at 9.40 T and 40 kHz MAS using a 0.05 s recycle delay and a Hahn echo pulse sequence. Spinning sidebands are marked with asterisks.

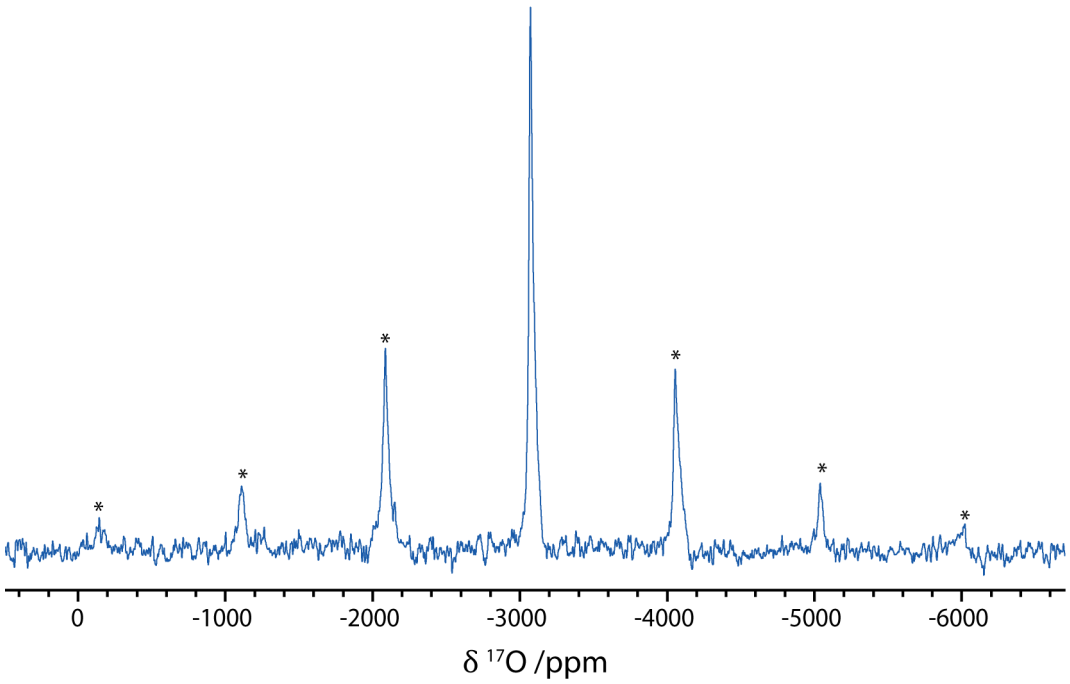

Figure S11: ^{17}O NMR spectrum of cubic Eu_2O_3 recorded at 7.05 T and 40 kHz MAS using a 0.15 s recycle delay and a Hahn echo pulse sequence. Spinning sidebands are marked with asterisks.

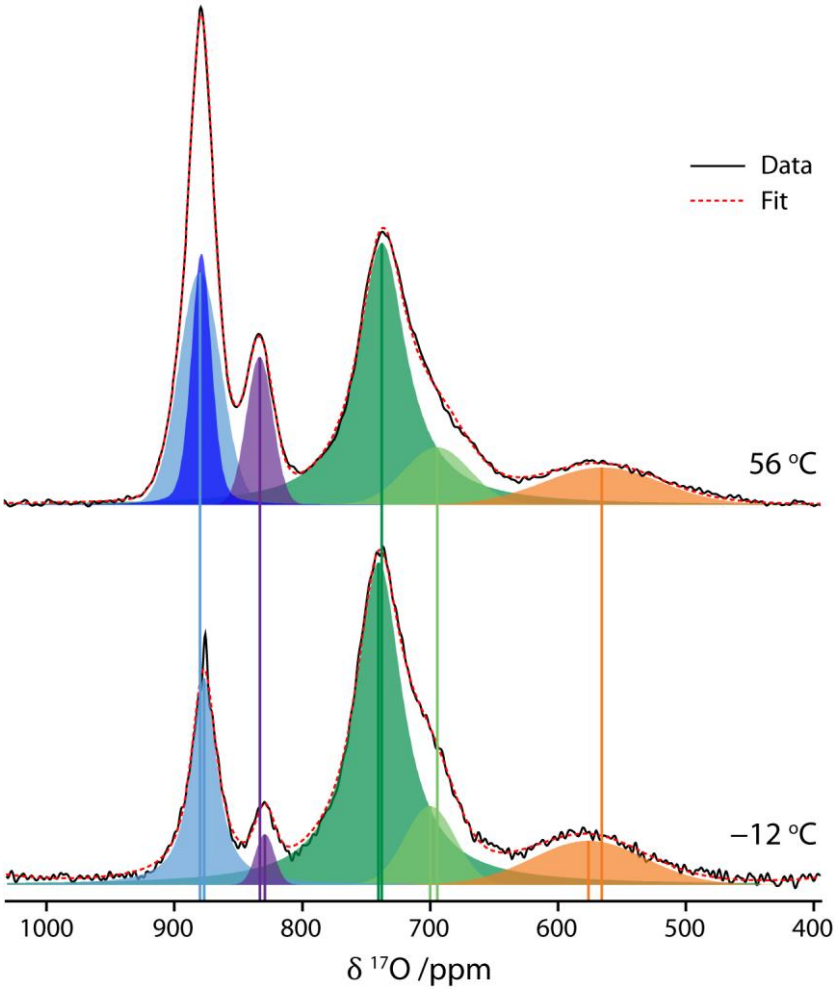

Figure S12: ^{17}O NMR spectra of 15 at% Sm-substituted CeO_2 at two different temperatures, recorded with a Hahn echo pulse sequence and a 1 s recycle delay. The high temperature spectrum was recorded at 7.05 T and 40 kHz MAS, while the low temperature spectrum was recorded at 4.70 T and 14 kHz MAS with liquid nitrogen cooled bearing gas. The evolution of chemical shift of the resonances is highlighted and there is also variation in the intensity of the two signals at highest frequency due to changes in the T_1 constants (see main text).

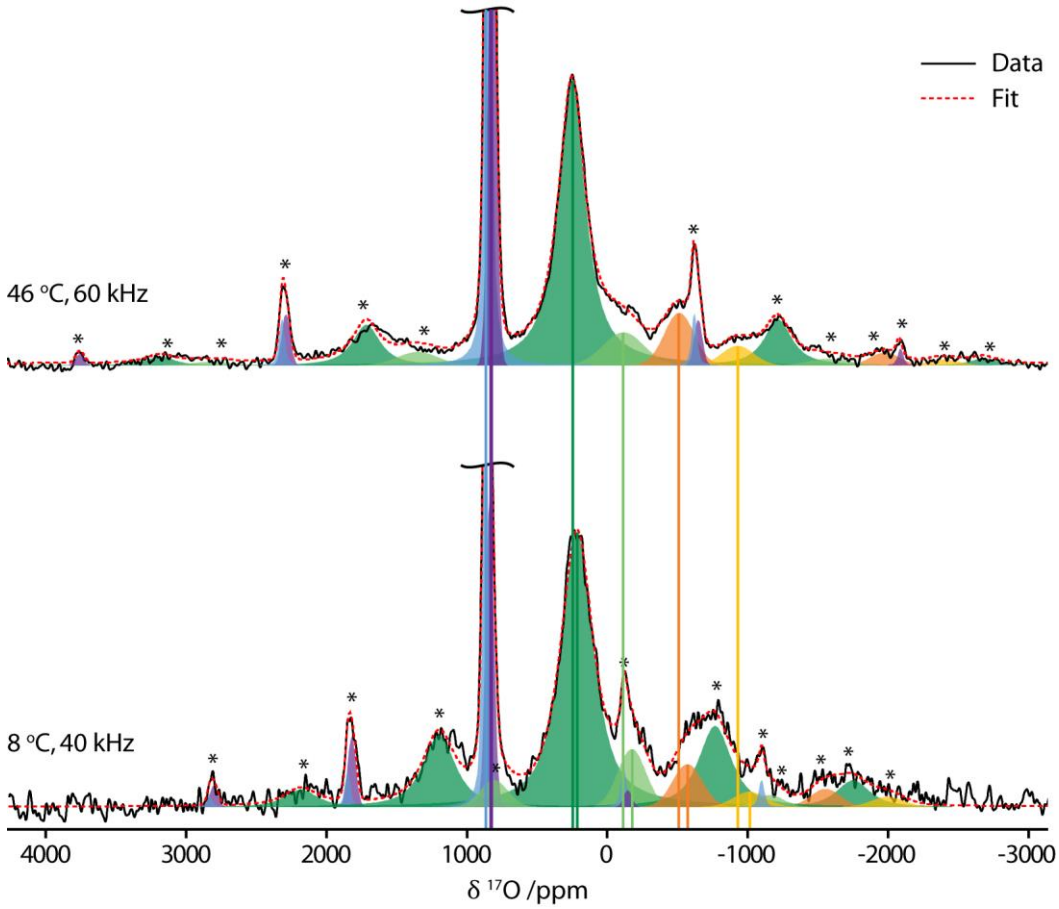

Figure S13: ^{17}O NMR spectra of 15 at% Eu-substituted CeO_2 at two different temperatures, recorded at 7.05 T with a 1 s recycle delay using a Hahn echo pulse sequence. The higher temperature spectrum was recorded at 60 kHz MAS and the lower temperature spectrum at 40 kHz MAS with the application of cooled nitrogen gas. The evolution of the chemical shifts is highlighted, although there is a significant error in determining the position of the lowest frequency isotropic resonance due to overlapping sidebands.

4 ^{17}O Enrichment Quantification

To estimate the degree of ^{17}O enrichment for the samples, a quantitative ^{17}O NMR spectrum of natural isotopic abundance H_2O was recorded at 9.40 T with a 1.9 mm probe, allowing a comparison to be made with the samples which were recorded using the same combination. From the ratios of the total integrated spectral intensities, the enrichments were estimated as shown in Table S3. Due to the averaging of the C_Q of H_2O in the liquid state by molecular tumbling, the central and satellite transitions are coincident, whereas for the solid samples the satellite transitions are anisotropically broadened and not all of the intensity is measured experimentally; consequently, the enrichment is likely to be underestimated to some extent by this method.

As can be seen, the enrichment of the cubic Sm_2O_3 sample, which was enriched at 750 °C, is nearly ideal within the error in the quantification (the gas is 70% enriched, and there are approximately equal amounts of oxygen in the sample and the gas, resulting in a factor of half). The monoclinic samples which were enriched at 1200 °C, on the other hand, have almost two orders of magnitude lower levels of enrichment. This can be ascribed to exchange of the ^{17}O with the ^{16}O in the quartz tube at this high temperature and suggests that an alternative methodology should be developed to improve the efficiency of high temperature enrichment. Nevertheless, isotopic enrichment of at least an order of magnitude is achieved, permitting the ^{17}O NMR spectra of the high temperature phases to be recorded and assigned, which would not have been feasible at natural abundance.

Table S3: Approximate ^{17}O enrichment level for different lanthanide oxide samples.

Sm_2O_3 Monoclinic	Eu_2O_3 Monoclinic	Sm_2O_3 Cubic
0.8%	0.3%	40%

5 DFT Calculations

The ^{17}O NMR parameters for the monoclinic Y_2O_3 phase (isostructural to monoclinic Sm_2O_3 and Eu_2O_3)[1] were calculated with the CASTEP code using a 700 eV energy cut-off and a <0.03 $Å^{-1}$ Monkhorst-Pack *k*-mesh sampling.[2–4] On-the-fly pseudopotentials with the PBE functional were used. The structure was fully relaxed using the CASTEP default convergence criteria and a 10^{-5} eV energy convergence limit. The calculated chemical shieldings were converted to chemical shifts using the previously determined relation $\delta_{iso} = 223.7 - 0.888\times\sigma_{iso}$.[5] The calculated chemical shifts and quadrupolar coupling constants (Table S4) are in good agreement with the experimental values of Florian et al.,[1] with the exception that the experimental assignment of O2 and O4 appears to be incorrect and should be reversed; this assignment by Florian et al. was tentatively based on the trend in average Y–O bond length, as it was not possible to calculate chemical shifts at the time, so this minor error is not unexpected.

Table S4: DFT-calculated ^{17}O chemical shifts and quadrupolar coupling constants of oxygen sites in monoclinic Y_2O_3. Experimental values are from Florian et al.[1]

Site	δ_{iso} (calc) /ppm	δ_{iso} (exp) /ppm	C_Q (calc) /MHz	C_Q (exp) /MHz	Coordination
O1	323.5	313	2.0	1.8	Square pyramidal (5)
O2	375.3	383	0.7	0.6	~Tetrahedral (4)
O3	356.0	346	1.0	1.2	Trigonal pyramidal (4)
O4	382.2	377	0.5	0.7	~Tetrahedral (4)
O5	255.5	242	0.9	0.8	~Octahedral (6)

Table S5: Lattice parameters of experimental and DFT-relaxed monoclinic structures of Sm_2O_3 and Eu_2O_3. Experimental structures were obtained from the ICSD with collection codes 34291 (Sm_2O_3)[6] and 8056 (Eu_2O_3)[7].

	Expt	Hyb20	Hyb35
Monoclinic Sm_2O_3			
a / Å	14.177	14.198	14.163
b / Å	3.633	3.659	3.648
c / A	8.847	8.880	8.861
β / deg	99.96	99.36	99.34
Monoclinic Eu_2O_3			
a / Å	14.111	14.173	14.122
b / Å	3.602	3.621	3.615
c / A	8.808	8.864	8.826
β / deg	100.037	99.597	99.532

Table S6: DFT-calculated isotropic hyperfine coupling constants (A_{iso}), quadrupolar coupling constants (C_Q), and the quadrupolar asymmetry parameter η_Q for the monoclinic phase of Sm_2O_3.

Monoclinic Sm_2O_3						
	Hyb20			Hyb35		
Site	A_{iso} / MHz	C_Q / MHz	η_Q	A_{iso} / MHz	C_Q / MHz	η_Q
O1 (4*i*)	−3.78	1.04	0.14	−3.48	1.34	0.31
O2 (4*i*)	−4.92	0.74	0.28	−4.44	0.67	0.35
O3 (4*i*)	−3.60	1.19	0.74	−3.36	1.09	1.00
O4 (4*i*)	−4.38	0.18	0.08	−4.02	0.26	0.91
O5 (2*e*)	−2.22	0.25	0.89	−2.04	0.15	0.24

Table S7: DFT-calculated isotropic hyperfine coupling constants (A_{iso}), quadrupolar coupling constants (C_Q), and the quadrupolar asymmetry parameter η_Q for the monoclinic phase of Eu_2O_3.

Monoclinic Eu_2O_3						
	Hyb20			Hyb35		
Site	A_{iso} / MHz	C_Q / MHz	η_Q	A_{iso} / MHz	C_Q / MHz	η_Q
O1 (4*i*)	−2.16	1.38	0.38	−2.04	1.57	0.41
O2 (4*i*)	−4.68	0.12	0.69	−4.02	0.37	0.41
O3 (4*i*)	−3.12	0.45	0.42	−2.64	0.67	0.79
O4 (4*i*)	−3.24	0.48	0.78	−3.18	0.46	0.38
O5 (2*e*)	−2.16	0.42	0.43	−2.04	0.17	0.29

The computed values of C_Q for Sm_2O_3 and Eu_2O_3 show a reasonable agreement to the size predicted from structural arguments (and also from the nutation behaviour): for Sm_2O_3, O2, O4, and O5 all show small values of C_Q (0.67, 0.26, and 0.15 MHz, respectively) whereas O3 and O1 show larger values of 1.34 and 1.09 MHz, A similar result is observed for Eu_2O_3, although the calculated C_Q for O3 is arguably smaller than expected (as compared to Sm_2O_3). Notably, in both systems Hyb20 gives a smaller dispersion of the computed C_Qs; based on the lattice parameters and the structural considerations as described in the main text, we conclude that the Hyb35-determined values are likely to be closer to the real values. The magnitude of the calculated hyperfine coupling constants A_{iso} is approximately correct (c.f. −2.206 MHz for cubic Eu_2O_3 from variable temperature NMR measurements, see main text), although the calculated values are slightly too large. There are also some differences in the predicted ordering of A_{iso} for each site between Sm_2O_3 and Eu_2O_3, but for both phases the O2 and O4 sites are predicted to be the most paramagnetically shifted.

6 Theoretical Shift Predictions

The temperature dependence of the paramagnetic shifts for cubic Sm_2O_3 and Eu_2O_3 was predicted by calculating the electron spin per unit field using the method of Golding and Halton.[8] First the contribution for each J level was calculated using

$$\frac{\langle S_z \rangle_J}{H} = -\mu_B \left[\frac{g_J(g_J-1)J(J+1)}{3kT} + \frac{2(g_J-1)(g_J-2)}{3\lambda} \right], \quad \text{(S1)}$$

where H is the magnetic field, μ_B is the Bohr magneton, k is the Boltzmann constant and $\lambda = \zeta/2S$ is the spin–orbit coupling constant, for which the values presented in Golding and Halton were used. These two terms represent the Curie and Van Vleck contributions, respectively, which are derived in §8. The Landé g-factor is given by

$$g_J = \frac{3}{2} + \frac{S(S+1) - L(L+1)}{2J(J+1)}, \tag{S2}$$

except when $J = 0$, as is this the case for the $^7F_0$ ground-state of Eu^{3+}, for which $g_J = L + 2$ (see §8.2).

The overall spin for the system was then found by a Boltzmann weighting of the levels:

$$\frac{\langle S_z \rangle}{H} = \frac{\sum \frac{\langle S_z \rangle_J}{H} (2J+1) \exp\left(-\frac{E_J}{kT}\right)}{\sum (2J+1) \exp\left(-\frac{E_J}{kT}\right)}, \tag{S3}$$

where $E_J = \lambda J(J+1)/2$.

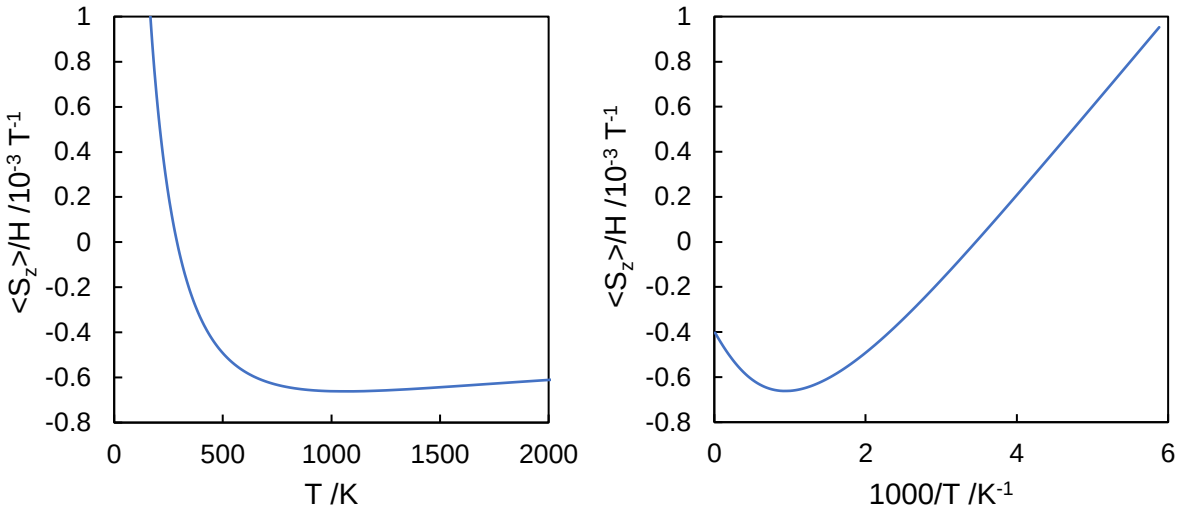

Figure S14: Calculated electron spin as a function of temperature and reciprocal temperature for Sm^{3+}.

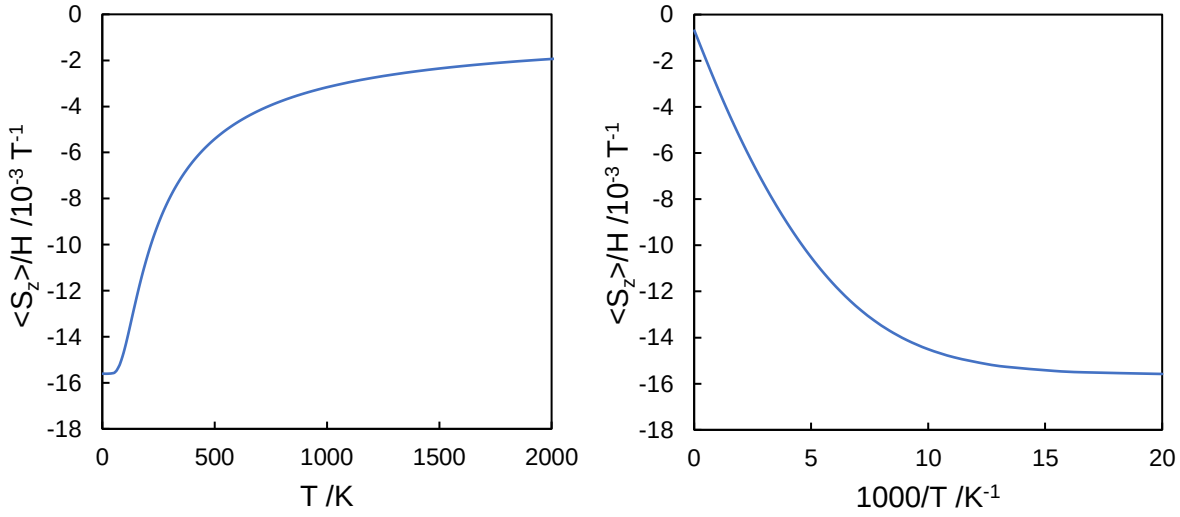

Figure S15: Calculated electron spin as a function of temperature and reciprocal temperature for Eu^{3+}.

The temperature dependences of the calculated spin for Sm^{3+} and Eu^{3+} are shown in Figure S14 and Figure S15, respectively; these reproduce the features observed in the variable temperature ^{17}O NMR experiments performed on cubic Sm_2O_3 and Eu_2O_3 (see main text). In particular, for Sm^{3+}, a minimum in the spin is predicted at ~1000 K, which is significantly higher than the minimum in the susceptibility (~400 K). This occurs because the Curie and Van Vleck paramagnetic terms can have different coefficients as well as different signs in the expressions for the magnetic susceptibility and the electron spin, respectively; paramagnetic shifts are only proportional to the magnetic susceptibility in the case

that only Curie(–Weiss) paramagnetism is present. For Eu^{3+}, on the other hand, the spin approaches a constant value below ~70 K due to the temperature-independent Van Vleck paramagnetism of the ground state, as expected.

7 Pseudo-contact Shift in Sm_2O_3

To determine whether a pseudo-contact shift could cause the observed discrepancies between the experimental shifts and calculated spin for Sm_2O_3, an estimate for the pseudo-contact shift was made using the Bleaney expression:[9,10]

$$\delta_{PCS} = -\frac{\mu_0 \mu_B^2 g_J^2 J(J+1)(2J-1)(2J+3)}{120\pi r^3 (kT)^2} \langle J||\alpha||J\rangle \times [(3\cos^2\theta - 1)A_2^0\langle r^2\rangle + \sin^2\theta \cos 2\phi\, A_2^2\langle r^2\rangle], \quad \text{(S4)}$$

where θ and ϕ are the angles relating the internuclear (*Ln*–O) vector and the principal axes of the crystal field splitting tensor, $A_2^0\langle r^2\rangle$ and $A_2^2\langle r^2\rangle$ give the axial and rhombic components of the crystal field splitting tensor in units of energy, and $\langle J||\alpha||J\rangle$ is the rank-2 spherical tensor operator reduced matrix element, which depends on S, L and J, but is independent of M_J. These factors have been tabulated for the ground levels of the lanthanides.[11,12] This formula only applies in the limit that the magnetic moment can be considered as a point dipole, which is undoubtedly invalid given the short *Ln*–O distance, however it is sufficient for a first approximation.

For the ground state of Sm^{3+}, the constant values are given by

$$\frac{\mu_0 \mu_B^2 g_J^2 J(J+1)(2J-1)(2J+3)}{120\pi k^2} \langle J||\alpha||J\rangle = 1.42 \times 10^{-9}\ \mathrm{m^3\ K^2\ J^{-1}},$$

and the total pseudo-contact shift can be written as a sum of the contributions from different Sm nearest neighbours:

$$\delta_{PCS} = -1.42 \times 10^{-9} \frac{W(T)}{T^2} \sum \frac{1}{r^3} [(3\cos^2\theta - 1)A_2^0\langle r^2\rangle + \sin^2\theta \cos 2\phi\, A_2^2\langle r^2\rangle]. \quad \text{(S5)}$$

$W(T)$ is an additional temperature-dependent factor determined by Bleaney due to the low-lying excited electronic states of Sm^{3+}, given by[10]

$$W(T) = 1 + a\frac{kT}{\Delta E} + b\left(\frac{kT}{\Delta E}\right)^2 + \frac{c(kT)^2}{\Delta E \Delta E'}, \quad \text{(S6)}$$

where ΔE is the energy separation of the ground state and the first excited state, and $\Delta E'$ is the energy separation of the first and second excited states. For Sm^{3+}, $a = -11.25$, $b = -3$ and $c = 4.5$, resulting in a negative $W(T)$ above 122 K and hence a change in the sign of the pseudo-contact shift. Equation (S5) is only valid up to around room temperature, above which the thermal population of excited states must also be considered, complicating the analysis significantly.

In cubic Sm_2O_3 ($Ia\bar{3}$) there are two different samarium sites at Wyckoff positions 8b and 24d: the former has three-fold symmetry, while the latter has two-fold symmetry. Each oxygen, in the general position 48e, has one 8b and three 24d Sm nearest neighbours.[13] The Sm–O distances and the crystal field splitting parameters, determined from optical measurements of single crystals of *Ln*-doped isomorphic cubic Y_2O_3, are shown in Table S8.

The crystal field tensor orientation for the 8b site is unambiguously determined by the three-fold symmetry axis, which is aligned at 8° to the Sm–O bond, yielding a pseudo-contact shift at 300 K of +42 ppm from equation (S5). The contributions from the 24d sites are more difficult to calculate, because the only requirement of the crystal field splitting tensor is that one principal axis is parallel to the two-fold symmetry axis, and as a result it is not possible without further experiments or calculations

to determine the angular factors in equation (S5). The maximum possible contribution from each of the three 24d Sm^{3+} nearest neighbours is ca. ±40 ppm, although the magnitudes are more likely to be significantly lower, especially as the axial and rhombic contributions can oppose. Without knowing the orientation of the 24d site crystal field splitting tensor, it is thus not possible to determine even the sign of the pseudo-contact shift, but nevertheless it can be seen that a pseudo-contact shift with a comparable magnitude to the experimentally observed chemical shifts (see main text) is feasible.

Table S8: Sm–O distances[13] and crystal field splitting parameters for the two Sm sites in cubic Sm_2O_3. The crystal field splitting of the 8b site is for Eu/Y_2O_3,[14] and that of the 24d site is for Sm/Y_2O_3.[15] The rhombic splitting of the axial 8b site is necessarily zero.

	r /Å	$A_2^0\langle r^2\rangle$ /cm^{-1}	$A_2^2\langle r^2\rangle$ /cm^{-1}
8b	2.311	586	–
24d	2.293, 2.445, 2.363	−105	−892

8 Derivation of the Lanthanide Spin

In the presence of low-lying electronic states, which are mixed into the ground state, the electron spin can be calculated using perturbation theory.[16,17] The wavefunction of a given level with total angular momentum quantum numbers J and M is, to first order,

$$\psi_{JM} = |JM\rangle - \sum_{J'M' \neq JM} \frac{\langle JM|\widehat{H}^{(1)}|J'M'\rangle}{E_{J'M'} - E_{JM}} |J'M'\rangle, \tag{S7}$$

where $|JM\rangle$ are the unperturbed wavefunctions and E_{JM} their energies. The perturbing Hamiltonian due to the applied field, H, which is assumed to be aligned along z, is given by

$$\widehat{H}^{(1)} = \mu_B(\hat{L}_z + 2\hat{S}_z)H = \mu_B(\hat{J}_z + \hat{S}_z)H. \tag{S8}$$

Because the states are eigenfunctions of $\hat{J}_z$, this term does not contribute to the off-diagonal matrix elements in (S7) and the perturbed wavefunction can be written

$$\psi_{JM} = |JM\rangle - \mu_B H \left(\sum_{J'M' \neq JM} \frac{\langle JM|\hat{S}_z|J'M'\rangle}{E_{J'M'} - E_{JM}} |J'M'\rangle \right). \tag{S9}$$

The spin of this level can then be calculated by

$$\langle S_z\rangle_{JM} = \langle JM|\hat{S}_z|JM\rangle - \mu_B H \left(\sum_{J'M' \neq JM} \frac{|\langle JM|\hat{S}_z|J'M'\rangle|^2}{E_{J'M'} - E_{JM}} \right). \tag{S10}$$

The first term can be derived by projecting the spin onto the total angular momentum. This is performed in §8.1 and yields

$$\langle S_z\rangle_{JM}^{(0)} = \langle JM|\hat{S}_z|JM\rangle = (g_J - 1)M, \tag{S11}$$

where the Landé g-factor is given in equation (S2).

The non-zero off-diagonal matrix elements can be shown to be[16,18]

$$\begin{aligned} \langle JM|\hat{S}_z|(J+1)\ M\rangle &= f(J+1)\sqrt{(J+1)^2 - M^2} \\ \langle JM|\hat{S}_z|(J-1)\ M\rangle &= f(J)\sqrt{J^2 - M^2} \end{aligned} \tag{S12}$$

$$f(J) = \sqrt{\frac{[J^2 - (L-S)^2][(L+S+1)^2 - J^2]}{4J^2(4J^2-1)}}.$$

Consequently, only adjacent states can be mixed, and only levels with the same M. (S10) can therefore be written with two terms for mixing of the higher and lower states respectively, noting that if either state does not exist, the corresponding value of $f(J)$ will be zero:

$$\begin{aligned}\langle S_z\rangle_{JM} &= \big(g_J - 1\big)M - \mu_B H\left(\frac{f(J+1)^2[(J+1)^2 - M^2]}{\lambda(J+1)} - \frac{f(J)^2[J^2-M^2]}{\lambda J}\right)\\ &= \langle S_z\rangle_{JM}^{(0)} + \langle S_z\rangle_{JM}^{(1)},\end{aligned} \tag{S13}$$

where λ is the spin–orbit coupling constant. The expectation value of the spin for a state J is then found by a Boltzmann weighting over the levels, M:

$$\langle S_z\rangle_J = \frac{\sum_{-J}^{+J}\langle S_z\rangle_{JM}\exp\left(\frac{-Mg_J\mu_B H}{kT}\right)}{\sum_{-J}^{+J}\exp\left(\frac{-Mg_J\mu_B H}{kT}\right)}. \tag{S14}$$

In the paramagnetic regime, $kT \gg g_J\mu_B H$, so that the denominator is approximately $2J+1$, and the exponential term in the numerator can be expanded to first order:

$$\begin{aligned}\langle S_z\rangle_J &= \frac{1}{2J+1}\sum_{M=-J}^{+J}\left(\langle S_z\rangle_{JM}^{(0)} + \langle S_z\rangle_{JM}^{(1)}\right)\left(1 - \frac{Mg_J\mu_B H}{kT}\right)\\ &= \frac{1}{2J+1}\sum_{M=-J}^{+J}\left(\langle S_z\rangle_{JM}^{(0)} - \frac{Mg_J\mu_B H\langle S_z\rangle_{JM}^{(0)}}{kT} + \langle S_z\rangle_{JM}^{(1)} + \frac{Mg_J\mu_B H\langle S_z\rangle_{JM}^{(1)}}{kT}\right).\end{aligned} \tag{S15}$$

The first and last terms sum to zero because they contain only odd powers of M. The second term is

$$\frac{1}{2J+1}\sum_{M=-J}^{+J}\left(-\frac{\mu_B H g_J\big(g_J-1\big)M^2}{kT}\right) = -\frac{\mu_B H g_J\big(g_J+1\big)}{3kT}J(J+1), \tag{S16}$$

using the fact that $\sum_{-J}^{+J}M^2 = \frac{1}{3}J(J+1)(2J+1)$. This is the Curie contribution to the spin.

Performing the same summations on the third term in (S15),

$$\begin{aligned}\frac{1}{2J+1}\sum_{M=-J}^{+J}\langle S_z\rangle_{JM}^{(1)} &= -\mu_B H\left[\frac{f(J+1)^2\left[(J+1)^2 - \frac{1}{3}J(J+1)\right]}{\lambda(J+1)} - \frac{f(J)^2\left[J^2 - \frac{1}{3}J(J+1)\right]}{\lambda J}\right]\\ &= -\frac{\mu_B H}{3\lambda}[f(J+1)^2(2J+3) - f(J)^2(2J-1)]\\ &= -\frac{\mu_B H}{3\lambda}\left\{\frac{[(J+1)^2 - (L-S)^2][(L+S+1)^2 - (J+1)^2](2J+3)}{4(J+1)^2(2J+1)(2J+3)}\right.\\ &\qquad\left. - \frac{[J^2-(L-S)^2][(L+S+1)^2 - J^2](2J-1)}{4J^2(2J+1)(2J-1)}\right\}\\ &= -\frac{\mu_B H}{3\lambda}\frac{1}{4J^2(J+1)^2(2J+1)}\{[(J+1)^2 - (L-S)^2][(L+S+1)^2 - (J+1)^2]J^2\\ &\qquad - [J^2-(L-S)^2][(L+S+1)^2 - J^2](J+1)^2\}\end{aligned}$$

$$= -\frac{\mu_B H}{3\lambda}\frac{1}{4J^2(J+1)^2(2J+1)}[(L-S)^2(L+S+1)^2 - J^2(J+1)^2][J^2-(J+1)^2]$$

$$= -\frac{\mu_B H}{3\lambda}\frac{1}{4J^2(J+1)^2}[(L-S)^2(L+S+1)^2 - J^2(J+1)^2]$$

$$= -\frac{\mu_B H}{3\lambda}\frac{[(S-L)(L+S+1)]^2 - [J(J+1)]^2}{4J^2(J+1)^2}$$

$$= -\frac{\mu_B H}{3\lambda}\frac{[S(S+1)-L(L+1)]^2 - [J(J+1)]^2}{4J^2(J+1)^2}$$

$$= -\frac{\mu_B H}{3\lambda}\frac{[S(S+1)-L(L+1)+J(J+1)][S(S+1)-L(L+1)-(J+1)]}{[2J(J+1)]^2}$$

$$= -\frac{\mu_B H(g_J-1)(g_J-2)}{3\lambda}$$

where, in the penultimate step, the numerator is a difference of two squares. This is the Van Vleck, temperature-independent contribution to the spin. Once again, the expression in terms of g_J is essentially fortuitous, rather than reflecting the fundamental importance of the Landé *g*-factor.

8.1 Calculating $\langle S_z \rangle_{JM}$

The Fermi contact shift is dependent on the z component of the spin, $\langle S_z \rangle_J$. When both spin, $\boldsymbol{S}$, and orbital, $\boldsymbol{L}$, angular momenta are present, in the Russell–Saunders coupling limit, they couple to give a total angular momentum, $\boldsymbol{J}$. The $\boldsymbol{S}$ and $\boldsymbol{L}$ can then be considered to be processing rapidly about $\boldsymbol{J}$, so that only their projection along $\boldsymbol{J}$ remains. To calculate $\langle S_z \rangle_J$, first the projection of $\boldsymbol{S}$ along $\boldsymbol{J}$ must be calculated:

$$\begin{aligned}\hat{\boldsymbol{S}}_J &= \left(\frac{\hat{\boldsymbol{S}}.\hat{\boldsymbol{J}}}{|\hat{\boldsymbol{J}}|}\right)\left(\frac{\hat{\boldsymbol{J}}}{|\hat{\boldsymbol{J}}|}\right) \\ &= \left(\frac{\hat{\boldsymbol{S}}.\hat{\boldsymbol{J}}}{|\hat{\boldsymbol{J}}|^2}\right)\hat{\boldsymbol{J}}.\end{aligned} \tag{S17}$$

Then to find $\hat{\boldsymbol{S}}.\hat{\boldsymbol{J}}$, consider $\left(\hat{\boldsymbol{S}}+\hat{\boldsymbol{J}}\right)^2$,

$$\begin{aligned}\left(\hat{\boldsymbol{S}}+\hat{\boldsymbol{J}}\right)^2 &= \hat{\boldsymbol{S}}^2 + \hat{\boldsymbol{J}}^2 + 2\hat{\boldsymbol{S}}.\hat{\boldsymbol{J}} \\ \hat{\boldsymbol{S}}.\hat{\boldsymbol{J}} &= \frac{1}{2}\left[\left(\hat{\boldsymbol{S}}+\hat{\boldsymbol{J}}\right)^2 - \hat{\boldsymbol{S}}^2 + \hat{\boldsymbol{J}}^2\right].\end{aligned} \tag{S18}$$

Using $\hat{\boldsymbol{J}} = \hat{\boldsymbol{L}} + \hat{\boldsymbol{S}}$,

$$\left(\hat{\boldsymbol{S}}+\hat{\boldsymbol{J}}\right)^2 = \left(\hat{\boldsymbol{L}}+2\hat{\boldsymbol{S}}\right)^2 = \hat{\boldsymbol{L}}^2 + 4\hat{\boldsymbol{S}}^2 + 4\hat{\boldsymbol{L}}.\hat{\boldsymbol{S}}, \tag{S19}$$

and, finding $\hat{\boldsymbol{L}}.\hat{\boldsymbol{S}}$ from

$$\begin{aligned}\hat{\boldsymbol{J}}^2 &= \left(\hat{\boldsymbol{L}}+\hat{\boldsymbol{S}}\right)^2 = \hat{\boldsymbol{L}}^2 + \hat{\boldsymbol{S}}^2 + 2\hat{\boldsymbol{L}}.\hat{\boldsymbol{S}} \\ \hat{\boldsymbol{L}}.\hat{\boldsymbol{S}} &= \frac{1}{2}\left[\hat{\boldsymbol{J}}^2 - \hat{\boldsymbol{L}}^2 - \hat{\boldsymbol{S}}^2\right],\end{aligned} \tag{S20}$$

then, substituting (S20) into (S19) and then into (S18),

$$\hat{\boldsymbol{S}}.\hat{\boldsymbol{J}} = \frac{1}{2}\left[\hat{\boldsymbol{J}}^2 + \hat{\boldsymbol{S}}^2 - \hat{\boldsymbol{L}}^2\right]. \tag{S21}$$

Substituting (S21) into (S17) and replacing the squared operators by their eigenvalues,

$$\widehat{\boldsymbol{S}}_J = \frac{J(J+1) + S(S+1) - L(L+1)}{2J(J+1)}\hat{\boldsymbol{J}} = (g_J - 1)\hat{\boldsymbol{J}}. \tag{S22}$$

As shown, this is typically written in terms of the Landé g-factor, equation (S2), although it should be stressed that this is simply for convenience, and does not imply that the spin arises from the magnetic moment given by g_J.

The z component of the spin is then found by projecting along z:

$$\begin{aligned} \hat{S}_z &= \widehat{\boldsymbol{S}}_{\boldsymbol{J}}.\boldsymbol{z} = (g_J - 1)\hat{\boldsymbol{J}}.\boldsymbol{z} = (g_J - 1)\hat{J}_z \\ \langle S_z \rangle_{JM} &= (g_J - 1)\langle J_z \rangle_{JM} = (g_J - 1)M \end{aligned} \tag{S23}$$

8.2 The Landé *g*-factor when $J = 0$

When $J = 0$, for instance in the ground state of Eu^{3+}, the Landé *g*-factor has an undefined value using the usual formula:

$$g_J = \frac{3}{2} + \frac{S(S+1) - L(L+1)}{2J(J+1)}. \tag{S24}$$

However, by exploiting the fact that it is only possible to have $J = 0$ if $J = S - L$, the formula can be rewritten,[12] and by refactorising the numerator, this allows cancellation of the division by zero:

$$\begin{aligned} g_J &= \frac{3}{2} + \frac{S(S+1) - L(L+1)}{2(S-L)(S-L+1)} \\ g_J &= \frac{3}{2} + \frac{(S-L)(S+L+1)}{2(S-L)(S-L+1)} \\ g_J &= \frac{3}{2} + \frac{(S+L+1)}{2(S-L+1)} \\ g_J &= 2 + L, \end{aligned} \tag{S25}$$

where in the last step $L = S$ is used, which must also be the case if $J = 0$.

9 References

(1) Florian, P.; Massiot, D.; Humbert, G.; Coutures, J. P. Etude Par RMN de ^{17}O et ^{89}Y Des Formes C et B de l'oxyde d'Yttrium Y_2O_3. *Comptes Rendus Académie des Sciences - Serie II*. 1995, pp 99–104.

(2) Clark, S. J.; Segall, M. D.; Pickard, C. J.; Hasnip, P. J.; Probert, M. J.; Refson, K.; Payne, M. C. First Principles Methods Using {CASTEP}. *Z. Krist.* **2005**, *220*, 567–570.

(3) Pickard, C. J.; Mauri, F. All-Electron Magnetic Response with Pseudopotentials: {NMR} Chemical Shifts. *Phys. Rev. B* **2001**, *63*, 245101.

(4) Yates, J. R.; Pickard, C. J.; Mauri, F. Calculation of NMR Chemical Shifts for Extended Systems Using Ultrasoft Pseudopotentials. *Phys. Rev. B* **2007**, *76*, 24401.

(5) Dervişoğlu, R.; Middlemiss, D. S.; Blanc, F.; Lee, Y.-L.; Morgan, D.; Grey, C. P. Joint Experimental and Computational ^{17}O and ^{1}H Solid State NMR Study of $Ba_2In_2O_4(OH)_2$ Structure and Dynamics. *Chem. Mater.* **2015**, *27* (11), 3861–3873.

(6) Cromer, D. T. The Crystal Structure of Monoclinic Sm_2O_3. *J. Phys. Chem.* **1957**, *61* (6), 753–

755.

(7) Yakel, H. L. A Refinement of the Crystal Structure of Monoclinic Europium Sesquioxide. *Acta Crystallogr. Sect. B* **1979**, *35* (3), 564–569.

(8) Golding, R.; Halton, M. A Theoretical Study of the ^{14}N and ^{17}O N.M.R. Shifts in Lanthanide Complexes. *Aust. J. Chem.* **1972**, *25* (12), 2577.

(9) Pell, A. J.; Pintacuda, G.; Grey, C. P. Paramagnetic NMR in Solution and the Solid State. *Prog. Nucl. Magn. Reson. Spectrosc.* **2019**, *111*, 1–271.

(10) Bleaney, B. Nuclear Magnetic Resonance Shifts in Solution Due to Lanthanide Ions. *J. Magn. Reson.* **1972**, *8* (1), 91–100.

(11) Elliott, R. J.; Stevens, K. W. H. The Theory of Magnetic Resonance Experiments on Salts of the Rare Earths. *Proc. R. Soc. London. Ser. A. Math. Phys. Sci.* **1953**, *218* (1135), 553–566.

(12) Abragam, A.; Bleaney, B. *Electron Paramagnetic Resonance of Transition Ions*; Clarendon Press: Oxford, 1970.

(13) Saiki, A.; Ishizawa, N.; Mizutani, N.; Kato, M. Structural Change of C-Rare Earth Sesquioxides Yb_2O_3 and Er_2O_3 as a Function of Temperature. *Yogyo Kyokai-Shi* **1985**, *93* (10), 649–654.

(14) Gruber, J. B.; Leavitt, R. P.; Morrison, C. A.; Chang, N. C. Optical Spectra, Energy Levels, and Crystal-field Analysis of Tripositive Rare-earth Ions in Y_2O_3 . IV. C_{3i} Sites. *J. Chem. Phys.* **1985**, *82* (12), 5373–5378.

(15) Chang, N. C.; Gruber, J. B.; Leavitt, R. P.; Morrison, C. A. Optical Spectra, Energy Levels, and Crystal-field Analysis of Tripositive Rare Earth Ions in Y_2O_3. I. Kramers Ions in C_2 Sites. *J. Chem. Phys.* **1982**, *76* (8), 3877–3889.

(16) Casey, A. T. Theoretical Principles of Paramagnetism. In *Theory and Applications of Molecular Paramagnetism*; Boudreaux, E. A., Mulay, L. N., Eds.; John Wiley & Sons: New York, 1976; pp 27–66.

(17) Van Vleck, J. H. *Handbook of Optics: The Theory of Electric and Magnetic Susceptibilities*; Oxford Univ. Press: Oxford, 1965.

(18) Condon, E. U.; Shortley, G. H. *The Theory of Atomic Spectra*; Cambridge University Press: Cambridge, 1935.